Radiological Imaging

The Theory of Image Formation,
Detection, and Processing

Volume 2

Harrison H. Barrett
William Swindell

*Department of Radiology
and
Optical Sciences Center
University of Arizona
Tucson, Arizona*

1981

11

Scattered Radiation

11.1 INTRODUCTION

We have largely ignored the effects of scattered radiation in the preceding chapters. For example, in discussing transmission imaging in Chapter 4 we considered a planar absorbing object described by a transmission function $g(\mathbf{r})$, and assumed that all x-ray photons travel in straight lines from source to detector. The interaction that caused $g(\mathbf{r})$ to be less than one was tacitly assumed to completely destroy the photon rather than redirect it to some other point on the detector. Similarly, in discussing emission imaging in Chapter 4, we again assumed only straight-line propagation. In Section 4.6.4 we somewhat superficially accounted for the attenuation of the gamma rays by interactions occurring in the portions of the patient's body lying between the radioactive organ and the detector, but paid no attention to the eventual fate of the scattered rays.

Neglect of scattered radiation can be an egregious error. From Fig. C.15 in Appendix C, we see that Compton scattering is the dominant interaction in soft tissue (essentially water) for photons in the energy range from about 40 keV to over 10 meV. Thus, contrary to our models, photons in this large energy range are *not* completely absorbed when they interact, but in fact may still contribute to the image after scattering. As we shall see in more detail later in this chapter, the detected scattered photons do not contribute much *useful* information to the image, but merely reduce its contrast and increase its noise level. In fact, scatter is often the *most* important factor limiting image quality and diagnostic accuracy. For this reason considerable effort has gone

into the elimination of scattered radiation through geometrical or electronic means. These efforts are described in Section 11.4.

On the other hand, a few researchers have been able to make good use of scattered and fluorescent radiation with imaging systems based on deliberate detection of scattered rather than unscattered radiation. This work is briefly treated in Section 11.5.

11.2   METHODS OF ANALYSIS FOR SCATTER PROBLEMS

11.2.1   Three Energy Regimes

The character of the Compton scattering process changes significantly as the photon energy is increased (see Appendix C). Although the boundaries are somewhat subjective, we may distinguish three separate energy regimes with properties summarized in Table 11.1. The low-energy regime below about 40 keV is of interest for mammography, radiography of the extremities, and nuclear scans with a few low-energy isotopes, notably ^{125}I. In this regime, photoelectric interactions predominate and scattering may be negligible. What scattering there is is elastic (small energy loss $\Delta\mathscr{E}$) and relatively isotropic $[d\sigma^{C}/d\Omega \propto (1 + \cos^{2}\theta)]$ (see Figs. C.10 and C.11).

In the important intermediate energy range, say 40–150 keV, Compton scattering dominates. It is usually a reasonable approximation to still use the low-energy form for $d\sigma^{C}/d\Omega$, but the energy loss $\Delta\mathscr{E}$ may well be signifi-

TABLE 11.1

Characteristics of Compton Scattering

Energy range	Dominant interaction in soft tissue	Angular dependence of differential scattering cross section	Photon energy loss on scattering
Low $\lesssim 40$ keV	Photoelectric	$\dfrac{d\sigma^{C}}{d\Omega} \propto (1 + \cos^{2}\theta)$	$\Delta\mathscr{E}$ very small
Medium approx. 40–150 keV	Compton	$\dfrac{d\sigma^{C}}{d\Omega} \propto (1 + \cos^{2}\theta)^{a}$	$\Delta\mathscr{E}$ may be significant
High 150 keV to 10 meV	Compton	Forward peaked	$\Delta\mathscr{E}$ large

^{a} This approximation works best for $\theta \lesssim 90°$ at the higher energies in this range (see Figs. C.10 and C.11).

cant. For example, at 150 keV the average $\Delta\mathscr{E}$ is 27 keV or 18% of the photon energy (Evans, 1968). At such energies it is therefore beginning to be possible to discriminate against scattered photons on the basis of their energies.

At energies above 150 keV, usually of interest only in nuclear medicine, the differential scattering cross section is definitely forward peaked, and the energy loss is large. For example, for a 511-keV gamma ray produced by positron annihilation, forward scattering is about five times more probable than backward scattering, and the average ΔE is 170 keV or 34% of the incident energy.

The other trend to be noted is that the total scattering cross section gradually decreases as the photon energy is increased (Fig. C.8).

These differences in scattering behavior influence the validity of various approximations that can be used to analyze the effects of scattered radiation, as well as the means available to control scatter in imaging systems.

11.2.2   The Single-Scatter Approximation

The simplest way to analyze scatter problems is to assume that none of the detected photons has undergone more than one scattering event. This would be a valid approximation if a typical dimension d of the body were small enough that $\mu^C d \lesssim 1$, where μ^C is the total Compton linear attenuation coefficient as defined in Appendix C. Unfortunately this condition is seldom satisfied in radiographic imaging since it requires that d be less than 5–10 cm. Alternatively, single scatter may still be a useful approximation in nuclear medicine systems with energy discrimination if, on the average, multiple scattering results in sufficient energy loss to place the photon well below the energy window. In any case, consideration of this approximation can still give useful qualitative insights even when it is not quantitatively justified.

To illustrate the use of the single-scatter approximation, let us consider the simple transmission imaging geometry shown in Fig. 11.1. A uniform slab of scattering medium of thickness L is irradiated by a very distant point source so that the incident beam is essentially collimated. We consider a thin pencil of rays of cross-sectional area $\mathscr{A}$; the scatter pattern for the whole beam may be found by superposing the patterns for many such pencils. We shall assume that the beam is monoenergetic and of sufficiently low energy that we may write [see (C.34)]

$$\frac{d\sigma^C}{d\Omega} = \frac{r_0^2}{2}(1 + \cos^2\theta), \tag{11.1}$$

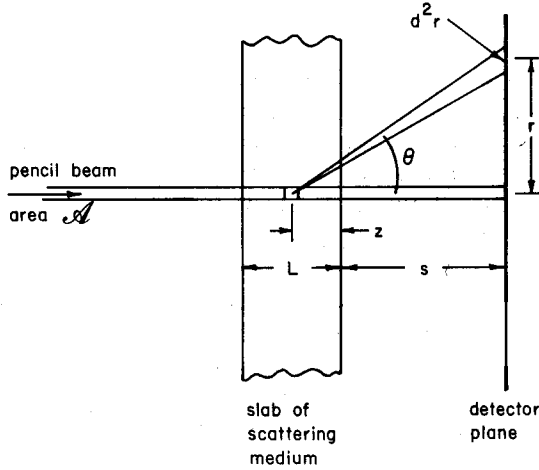where r_0 is the classical electron radius.

Fig. 11.1 Simple transmission-imaging arrangement in which a uniform slab is irradiated with a thin pencil beam.

If we consider a volume element $\mathscr{A}\,dz$ situated along the pencil at a distance z from the *exit* face of the slab, it receives an unscattered x-ray fluence of

$$\Phi(z) = \Phi_0 \exp[-\mu^{\text{tot}}(L - z)], \tag{11.2}$$

where μ^{tot} is the total linear attenuation coefficient and Φ_0 is the incident fluence. (Both $\Phi(z)$ and Φ_0 are measured in photons per unit area.) Of course, this element may also receive and rescatter photons that have already been scattered one or more times, but these photons are neglected in the single-scatter approximation.

The element $\mathscr{A}\,dz$ contains $n_e\,\mathscr{A}\,dz$ electrons, where n_e is the electron density (electrons per unit volume). The total number of photons per unit solid angle scattered by the volume element is

$$\Phi(z)\left(\frac{d\sigma^{\text{C}}}{d\Omega}\right)n_e\mathscr{A}\,dz. \tag{11.3}$$

A detector element of area d^2r located a distance r from the axis of the pencil subtends a differential solid angle (see Section 4.1) of

$$d\Omega = \frac{d^2r}{(s + z)^2}\cos^3\theta, \tag{11.4}$$

where

$$\theta = \tan^{-1}[r/(z + \hat{s})]. \tag{11.5}$$

The number of photons scattered in the direction of this detector element by the volume element $\mathscr{A}\,dz$ is obtained by multiplying (11.3) and (11.4). However, some of these photons may be attenuated before they emerge from the body. Since they must travel a distance $z\sec\theta$ from the scattering point to the exit face of the slab, the appropriate attenuation factor is

$$\exp(-\mu^{\text{tot}}z\sec\theta). \tag{11.6}$$

The total number of scattered photons received by the detector element d^2r is denoted by $h_s(\mathbf{r})\,d^2r$, where, as in previous chapters, the notation $h(\mathbf{r})$ expresses a number of photons per unit area in the detector plane. Combining (11.1), (11.4), and (11.6) and integrating over z to account for all scattering elements along the pencil, we have

$$h_s(\mathbf{r}) = \tfrac{1}{2}r_0^2 n_e \mathscr{A}\Phi_0 \int_0^L \exp[-\mu^{\text{tot}}(L-z)]$$

$$\cdot \exp[-\mu^{\text{tot}}z\sec\theta](1 + \cos^2\theta)\frac{\cos^3\theta}{(s+z)^2}\,dz. \tag{11.7}$$

In general, θ is a function of z through (11.5). However, if the air gap s is at least as large as L, then $\cos\theta$ varies very little with z. It is then an excellent approximation to set

$$\theta \approx \bar{\theta} \equiv \tan^{-1}[r/(s + \tfrac{1}{2}L)] \tag{11.8}$$

everywhere in the integrand. To the same order of approximation

$$(s + z)^2 \approx (s + \tfrac{1}{2}L)^2. \tag{11.9}$$

The integral in (11.7) is now trivial, and we have

$$h_s(\mathbf{r}) = \tfrac{1}{2}r_0^2 n_e \mathscr{A}\Phi_0 \exp(-\mu^{\text{tot}}L)\cos^3\bar{\theta}(1 + \cos^2\bar{\theta})(s + \tfrac{1}{2}L)^{-2}\frac{1 - \exp(-\mu'L)}{\mu'},$$

$$\tag{11.10}$$

where

$$\mu' \equiv \mu^{\text{tot}}(\sec\bar{\theta} - 1). \tag{11.11}$$

This expression is a complicated function of r through (11.8). The total detected photon density due to the single pencil beam is

$$h(\mathbf{r}) = h_s(\mathbf{r}) + h_u(\mathbf{r}), \tag{11.12}$$

where $h_u(\mathbf{r})$, the unscattered component, is given by

$$h_u(\mathbf{r}) = \Phi_0\exp(-\mu^{\text{tot}}L) = \Phi(L) \qquad (\mathbf{r}\text{ in beam area}). \tag{11.13}$$

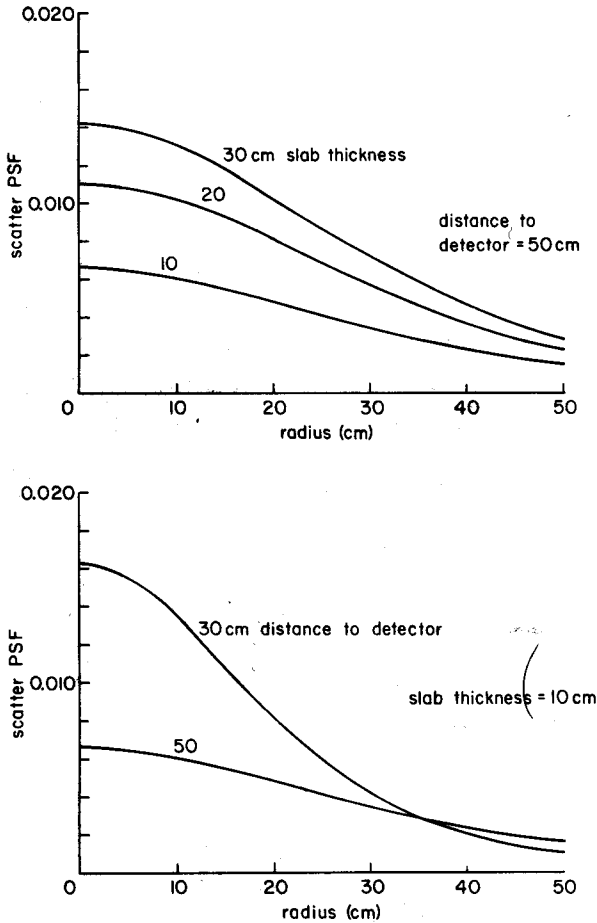Representative plots of $h_s(\mathbf{r})$ are given in Fig. 11.2.

Fig. 11.2 Plots of the scatter PSF $h_s(\mathbf{r})$ from (11.10) for various slab thicknesses L and distances to the detector s. The ordinates are in units of $\frac{1}{2}r_0^2 n_e \mathscr{A} \Phi_0 \exp(-\mu^{tot} L)$.

There are two important points to be noted from this result. The first is that scatter gives rise to broad, structureless wings around a point image. [The pattern $h(\mathbf{r})$ just calculated can be regarded as the image of a low-contrast pointlike object of area $\mathscr{A}$ located somewhere along the pencil.] Although these wings appear to have very low amplitude, they soon become significant as the number of pencils in the beam is increased. For a very broad beam, the total scattered flux at any point on the detector is proportional to the area integral of $h_s(\mathbf{r})$, so even very small wings are important if they extend out a long way.

The second point, to be seen by comparing (11.10) and (11.13), is that the relative importance of $h_s(\mathbf{r})$ can be reduced by the simple expedient of increasing the air gap s. Since we have assumed that the primary beam is collimated (i.e., the source is a long distance to the left of the slab), increasing s has no effect on $h_u(\mathbf{r})$ but decreases $h_s(\mathbf{r})$ by the factor of $1/(s + \frac{1}{2}L)^2$.

11.3   THE IMPORTANCE OF SCATTERED RADIATION

11.3.1   Deterministic Image Properties

Scattered radiation enters into the analytical description of a radiographic system in much the same way as septal penetration radiation (see Section 4.6.2). The overall PSF $p_{tot}(\mathbf{r})$ consists of a primary or unscattered component $p_{pri}(\mathbf{r})$ and a scatter component $p_{scat}(\mathbf{r})$. The primary PSF was calculated for various systems in Chapter 4. It represents the point image formed by photons that have not undergone any interactions, either in the patient's body or in the shielding and collimating structure of the imaging system. The scatter PSF, on the other hand consists of photons that have undergone one or more Compton scattering events. [$p_{scat}(\mathbf{r})$ is often shift variant, but we shall not acknowledge that fact in the notation.] Since the scattered and unscattered photons form two mutually exclusive classes, it follows that $p_{tot}(\mathbf{r})$ can be written as a simple sum, just as in the case of septal penetration:

$$p_{tot}(\mathbf{r}) = p_{pri}(\mathbf{r}) + p_{scat}(\mathbf{r}). \tag{11.78}$$

The general character of the scatter PSF was indicated in Section 11.2. As exemplified by Fig. 11.2, $p_{scat}(\mathbf{r})$ is a broad, slowly varying function. It is often a good approximation to represent it as a Gaussian of the form

$$p_{scat}(\mathbf{r}) = A_s T \exp(-\pi \beta_s^2 r^2), \tag{11.79}$$

where T is the exposure time and A_s and β_s are parameters depending on the photon energy, and the properties of the scattering medium and the imaging system. (A_s has dimensions of 1/area, while β_s is a spatial frequency, dimensions 1/length.) One can, for example, obtain the Gaussian representation by using the expansion

$$\sec \theta \approx 1 + \tfrac{1}{2}\theta^2 \tag{11.80}$$

in (11.6)

Since the Fourier transform of a Gaussian is also a Gaussian, the transfer function for the scattered radiation is given by

$$P_{scat}(\boldsymbol{\rho}) = \mathscr{F}_2\{p_{scat}(\mathbf{r})\} = P_{scat}(0) \exp(-\pi \rho^2 / \beta_s^2), \tag{11.81}$$

where, by the central ordinate theorem (B.15),

$$P_{scat}(0) = \int_\infty p_{scat}(\mathbf{r})\, d^2r = A_s T / \beta_s^2. \tag{11.82}$$

We may define a scatter-to-primary ratio (SPR) by

$$\text{SPR} = \frac{\int_\infty p_{\text{scat}}(\mathbf{r}) \, d^2 r}{\int_\infty p_{\text{pri}}(\mathbf{r}) \, d^2 r} = \frac{P_{\text{scat}}(0)}{P_{\text{pri}}(0)}. \tag{11.83}$$

Even if the object is more complicated than a single point, the SPR is still given by (11.83) if the PSFs are shift invariant. To demonstrate this point, note that

$$\frac{\int_\infty [p_{\text{scat}}(\mathbf{r}) ** f(\mathbf{r})] \, d^2 r}{\int_\infty [p_{\text{pri}}(\mathbf{r}) ** f(\mathbf{r})] \, d^2 r} = \frac{P_{\text{scat}}(0)F(0)}{P_{\text{pri}}(0)F(0)} = \text{SPR}. \tag{11.84}$$

On the other hand, if either p_{pri} or p_{scat} is shift variant, then SPR is a function of the object distribution $f(\mathbf{r})$.

As one way of investigating $p_{\text{tot}}(\mathbf{r})$, let us assume that $p_{\text{pri}}(\mathbf{r})$ can also be described by a Gaussian:

$$p_{\text{pri}}(\mathbf{r}) = A_p T \exp(-\pi \beta_p^2 r^2). \tag{11.85}$$

This would be a good approximation for a transmission radiography system with a Gaussian focal spot, or for a nuclear medicine system where p_{pri} is dominated by the detector response, which is often Gaussian. In other cases, the main virtue of (11.85) is analytic simplicity. With this all-Gaussian model, $\text{SPR} = A_s \beta_p^2 / A_p \beta_s^2$, and the overall MTF is given by

$$\text{MTF}_{\text{tot}} = \frac{P_{\text{tot}}(\rho)}{P_{\text{tot}}(0)} = \frac{P_{\text{pri}}(\rho) + P_{\text{scat}}(\rho)}{P_{\text{pri}}(0) + P_{\text{scat}}(0)}$$

$$= (1 + \text{SPR})^{-1} [\exp(-\pi \rho^2 / \beta_p^2) + \text{SPR} \cdot \exp(-\pi \rho^2 / \beta_s^2)]. \tag{11.86}$$

This function is plotted in Fig. 11.4. Since the scatter MTF is always much narrower than the primary MTF ($\beta_s \ll \beta_p$), the effect of scatter is to reduce the contrast at intermediate spatial frequencies in the range between β_s and β_p. For frequencies small compared to β_p but large compared to β_s, the contrast reduction is

$$\frac{P_{\text{tot}}(\rho)}{P_{\text{pri}}(\rho)} \approx \frac{1}{1 + \text{SPR}}, \qquad \beta_s \ll \rho \ll \beta_p. \tag{11.87}$$

As an example of the applicability of this result, consider a typical transmission radiography system where β_p may be 5 mm^{-1}. The scatter PSF will usually have a width of many centimeters, so that $\beta_s \approx 0.01$ mm^{-1} is not unreasonable. Then (11.87) shows that sinusoidal objects with spatial periods in the range from a millimeter or so to a few centimeters will have their
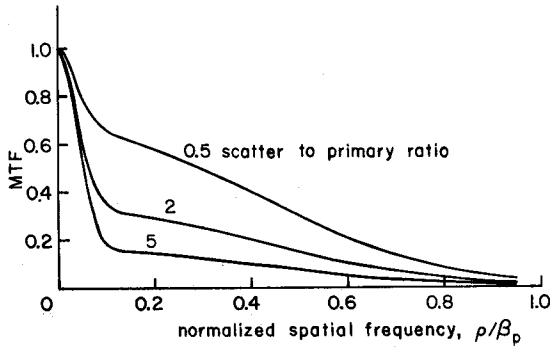
Fig. 11.4 MTF for a model in which both the scatter PSF and the primary PSF are Gaussian functions.
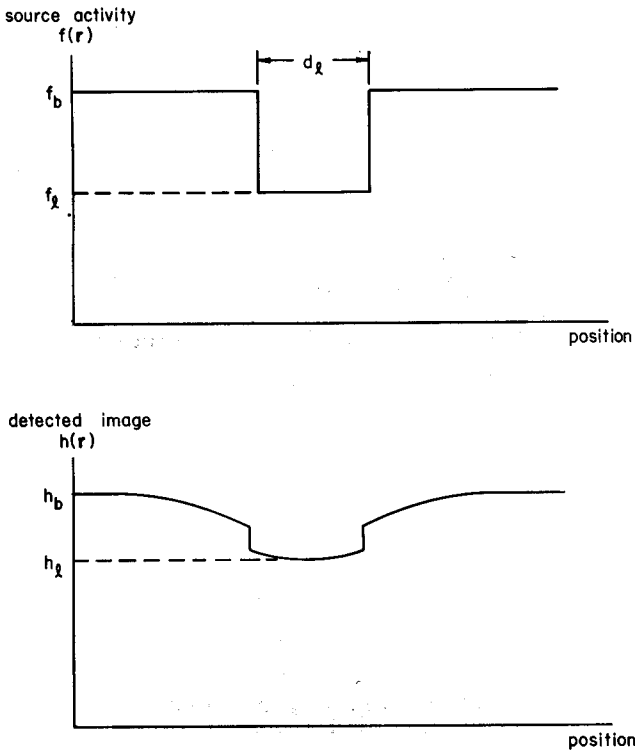

Fig. 11.5 Top: Broad, uniform source with a cold lesion of diameter d_l. Bottom: Image of the source when the only image degradation is a Gaussian scatter PSF.

modulation or contrast reduced by a factor of $(1 + \text{SPR})^{-1}$. If no precautions are taken, SPR can easily range up to 10.

Of course, scatter problems can also be analyzed entirely in the space domain. To illustrate, let us consider the nuclear-medicine problem illustrated in Fig. 11.5, which is intended to represent a liver scan with a cold, low-contrast lesion in a uniform background. The source function is

$$f(\mathbf{r}) = f_b + (f_l - f_b)\,\text{circ}(2r/d_l), \tag{11.88}$$

where subscripts b and l refer to "background" and "lesion." The detected image $h(\mathbf{r})$ is $f(\mathbf{r})$ filtered with $p_{tot}(\mathbf{r})$. Assuming unit magnification, we may write

$$h(\mathbf{r}) = f(\mathbf{r}) ** p_{tot}(\mathbf{r}) = f(\mathbf{r}) ** p_{pri}(\mathbf{r}) + f(\mathbf{r}) ** p_{scat}(\mathbf{r}). \tag{11.89}$$

We continue to use the Gaussian model for both p_{pri} and p_{scat}, and assume that the primary resolution is adequate to sharply image the lesion. The primary PSF can then be approximated by a delta function,

$$p_{pri}(\mathbf{r}) \approx (A_p T/\beta_p^2)\,\delta(\mathbf{r}). \tag{11.90}$$

By contrast, we assume that the scatter PSF is so broad that the lesion is completely unresolved by the scattered radiation, or $\beta_s d_l \ll 1$. This means that when p_{scat} is convolved with $f(\mathbf{r})$, the circ function in (11.88) can be treated as a delta function, so that

$$p_{scat}(\mathbf{r}) ** \text{circ}(2r/d_l) \approx \tfrac{1}{4}\pi d_l^2 p_{scat}(\mathbf{r}). \tag{11.91}$$

However, the background is assumed to be absolutely uniform, extending to infinity, so the approximation of (11.91) does not apply to the background term.

With these approximations, (11.89) becomes

$$h(\mathbf{r}) \approx (A_p T/\beta_p^2)[f_b - \Delta f\,\text{circ}(2r/d_l)]$$
$$+ (A_s T/\beta_s)^2 f_b - \Delta f(\pi d_l^2/4)A_s T\exp(-\pi\beta_s^2 r^2), \tag{11.92}$$

where $\Delta f = f_b - f_l$. Referring to Fig. 11.5, we see that

$$h_b = h(\mathbf{r} \to \infty) = \left(\frac{A_p T}{\beta_p^2} + \frac{A_s T}{\beta_s^2}\right)f_b, \tag{11.93}$$

$$h_l = h(\mathbf{r} = 0) = h_b - \Delta f\left(\frac{A_p T}{\beta_p^2} + \frac{\pi d_l^2}{4}A_s T\right). \tag{11.94}$$

Hence, with (11.82) and (11.83),

$$\frac{\Delta h}{h_b} = \frac{h_b - h_l}{h_b} = \frac{1 + (\tfrac{1}{4}\pi d_l^2)\beta_s^2\,\text{SPR}}{1 + \text{SPR}} \cdot \frac{\Delta f}{f_b}. \tag{11.95}$$

Once again, the contrast is reduced by a factor of $(1 + \text{SPR})^{-1}$. The extra term in the numerator, $(\pi d_l^2/4)\beta_s^2 \text{ SPR}$, is probably negligible since we have assumed that $\beta_s d_l \ll 1$. However, the interpretation of this extra term is interesting. It represents the small fraction of the object spectrum that falls within the passband of the low-pass filter $p_{\text{scat}}(\mathbf{r})$. It does not appear in (11.87) because that equation applies to an object spectrum that is nonzero only at the specific frequency ρ, rather than a spectrum like $\mathscr{F}_2\{\text{circ}(2r/d_l)\}$ that extends from zero to some finite "cutoff" frequency (of order $1/d_l$ in this case).

The procedures of this section can in principle be extended to more complicated objects and more general PSFs, but the analysis quickly becomes very involved. A particular difficulty arises when three-dimensional objects are considered, so that p_{scat} is not only shift variant within a single object plane, but also depends parametrically on the depth z of the plane. However, the main conclusion reached in this section remains generally valid: the contrast is always reduced by scatter.

11.3.2 Noise Due to Scatter → *Optional section*

It is straightforward to include the effects of scatter in the noise analysis presented in Chapter 10. The noise in a processed image $\mathbf{u}^\dagger(\mathbf{r})$ depends on the PSF of the processing filter, $p_f(\mathbf{r})$, and on the mean spatial density of detected photons $h(\mathbf{r})$. It makes no difference whether a photon that contributes to $h(\mathbf{r})$ traveled to the detector plane in a straight line from the source or suffered one or more interactions en route. [We are assuming here that all photons are recorded in a binary fashion so that they either contribute to $h(\mathbf{r})$ or they do not. There would be an additional noise if photons of different energy contributed differently to the image (see Section 5.5.1).] Quite generally, the noise variance in $\mathbf{u}^\dagger(\mathbf{r})$ is given by (10.10). If we divide $h(\mathbf{r})$ into primary and scattered components, this equation reads

$$\sigma_{u^\dagger}^2(\mathbf{r}) = [p_f(\mathbf{r})]^2 ** [h_{\text{pri}}(\mathbf{r}) + h_{\text{scat}}(\mathbf{r})]. \tag{11.96}$$

Similarly, the mean value of $\mathbf{u}^\dagger(\mathbf{r})$ is given by (10.11) as

$$\langle \mathbf{u}^\dagger(\mathbf{r}) \rangle = p_f(\mathbf{r}) ** [h_{\text{pri}}(\mathbf{r}) + h_{\text{scat}}(\mathbf{r})]. \tag{11.97}$$

If we define SNR in the same way as in Chapter 10, we have

$$\text{SNR}(\mathbf{r}) = \frac{\langle \mathbf{u}^\dagger(\mathbf{r}) \rangle}{\sigma_{u^\dagger}(\mathbf{r})} = \frac{p_f ** (h_{\text{pri}} + h_{\text{scat}})}{[p_f^2 ** (h_{\text{pri}} + h_{\text{scat}})]^{1/2}}. \tag{11.98}$$

If both h_{pri} and h_{scat} are slowly varying by comparison with p_f and p_f^2, this equation reduces to

$$\text{SNR}(\mathbf{r}) \approx (A_{\text{eff}})^{1/2}[h_{\text{pri}}(\mathbf{r}) + h_{\text{scat}}(\mathbf{r})]^{1/2}, \tag{11.99}$$

where A_{eff} is the effective noise-averaging area given by [cf. (10.151)]

$$A_{\text{eff}} = \left(\int_\infty p_f(\mathbf{r})\, d^2\mathbf{r} \right)^2 \bigg/ \int_\infty [p_f(\mathbf{r})]^2\, d^2r. \qquad (11.100)$$

The SNR is thus the square root of the total counts in the area A_{eff}.

Many authors adopt a different definition for SNR in scatter problems. They argue that the scatter photons contribute no useful "signal" information, so the signal should be defined as just $p_f(\mathbf{r}) ** h_{\text{pri}}(\mathbf{r})$. With this definition we have

$$\text{SNR}'(\mathbf{r}) \equiv \frac{p_f(\mathbf{r}) ** h_{\text{pri}}(\mathbf{r})}{\sigma_{u\dagger}(\mathbf{r})} \approx (A_{\text{eff}})^{1/2}\, \frac{h_{\text{pri}}(\mathbf{r})}{[h_{\text{pri}}(\mathbf{r}) + h_{\text{scat}}(\mathbf{r})]^{1/2}}$$

$$= [A_{\text{eff}} h_{\text{pri}}(\mathbf{r})]^{1/2} \left(1 + \frac{h_{\text{scat}}(\mathbf{r})}{h_{\text{pri}}(\mathbf{r})} \right)^{-1/2}, \qquad (11.101)$$

where the last two expressions again require that h_{pri} and h_{scat} vary slowly over the area A_{eff}.

The quantity $h_{\text{scat}}(\mathbf{r})/h_{\text{pri}}(\mathbf{r})$ is a *local* scatter-to-primary ratio, not to be confused with the integral SPR given by (11.83) or (11.84). Only in the rather extreme case where the object $f(\mathbf{r})$ is slowly varying compared to the broad scatter PSF $p_{\text{scat}}(\mathbf{r})$ can we approximate $h_{\text{scat}}(\mathbf{r})/h_{\text{pri}}(\mathbf{r})$ by SPR.

Whichever definition is used, the SNR depends greatly on the nature of the object distribution. For example, consider a scintillation camera of unit magnification viewing a source distribution $f(\mathbf{r})$ in a scattering medium. If $f(\mathbf{r})$ is a point source $\delta(\mathbf{r})$, we have

$$h_{\text{pri}}(\mathbf{r}) = \delta(\mathbf{r}) ** p_{\text{pri}}(r) = p_{\text{pri}}(\mathbf{r}), \qquad (11.102)$$

$$h_{\text{scat}}(\mathbf{r}) = \delta(\mathbf{r}) ** p_{\text{scat}}(\mathbf{r}) = p_{\text{scat}}(\mathbf{r}). \qquad (11.103)$$

On the Gaussian model of Section 11.3.1, the local scatter-to-primary ratio at the center of the point image is just

$$\frac{h_{\text{scat}}(0)}{h_{\text{pri}}(0)} = \frac{p_{\text{scat}}(0)}{p_{\text{pri}}(0)} = \frac{A_s}{A_p} = \frac{\beta_s^2}{\beta_p^2} \cdot \text{SPR}. \qquad (11.104)$$

Since $\beta_p^2 \gg \beta_s^2$, the local scatter-to-primary ratio at $\mathbf{r} = 0$ may be much less than one even when the integral ratio SPR is larger than one. This means that the scattered photons are spread out over the detector plane and do not seriously affect a point image.

The situation is very different for larger objects. We now let $f(\mathbf{r})$ be a uniform disk,

$$f(\mathbf{r}) = f_0 \operatorname{circ}(2r/d_0). \qquad (11.105)$$

If we assume that $\beta_s \ll 1/d_0 \ll \beta_p$, we find

$$h_{\text{pri}}(\mathbf{r}) \approx (f_0 A_p T/\beta_p^2)\,\text{circ}(2r/d_0), \tag{11.106}$$

$$h_{\text{scat}}(\mathbf{r}) \approx (\pi d_0^2/4)(f_0 A_s T)\exp(-\pi\beta_s^2 r^2), \tag{11.107}$$

and

$$\frac{h_{\text{scat}}(0)}{h_{\text{pri}}(0)} = \frac{\pi}{4}\frac{A_s}{A_p}\beta_p^2 d_0^2 = \tfrac{1}{4}\pi\beta_s^2 d_0^2 \;\text{SPR}. \tag{11.108}$$

Thus the local scatter ratio at the center of the disk image increases rapidly as the disk diameter d_0 is increased, and the SNR degrades accordingly.

The same conclusion applies to transmission imaging, except that there d_0 should be interpreted as the diameter of the irradiated portion of the object.

11.4   CONTROL OF SCATTERED RADIATION

11.4.1   Transmission Imaging

Scattered radiation may be minimized in transmission radiography by:

1. limiting the area of the incident beam;
2. using an air gap between the scattering medium and the detector;
3. using a collimating grid between the scattering medium and the detector;
4. optimizing the spectrum of the incident x rays.

The efficacy of the first two methods can be seen from the single-scatter model introduced in Section 11.2.2. There we showed that a small pencil beam of x rays produces a broad exposure pattern on the detector. As long as this exposure pattern is broader than the incident beam, the total scatter exposure at any point is directly proportional to the beam area. Of course the beam area must be large enough to encompass everything of medical interest in the region being imaged, but making it larger than necessary increases the scatter fraction as well as the integrated patient dose.

The single-scatter discussion also showed the advantage of an air gap between the patient and the detector. Each volume element in the patient's body acts as a source of scattered radiation, and the detected scatter intensity falls off as the inverse square of the distance from the volume element to the detector. In Fig. 11.6 this distance is approximately the perpendicular distance s_2. Unscattered radiation, on the other hand, falls off approxi-
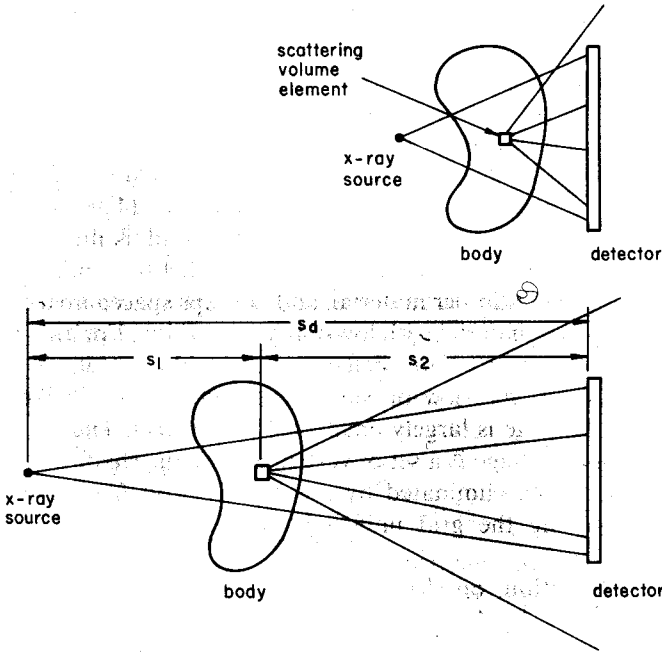
Fig. 11.6   Illustration of how an air gap can reduce the scatter-to-primary ratio in transmission radiography.

mately as $1/s_d^2$, where s_d is the perpendicular distance from the source to the detector plane. The local scatter-to-primary ratio thus varies as $(s_d/s_2)^2$.

Similar conclusions hold for the integral SPR. A circular detector of diameter d_{det} subtends a solid angle Ω_s from an axial scattering element, where

$$\Omega_s = 2\pi(1 - \cos\theta_s), \qquad (11.109)$$

$$\theta_s = \tan^{-1}(d_{det}/2s_2). \qquad (11.110)$$

Similarly, the solid angle subtended from the primary x-ray source is

$$\Omega_p = 2\pi(1 - \cos\theta_p), \qquad (11.111)$$

$$\theta_p = \tan^{-1}(d_{det}/2s_d). \qquad (11.112)$$

For a given scattering medium, the SPR is proportional to Ω_s/Ω_p. If the angles θ_p and θ_s are small, we have

$$\frac{\Omega_s}{\Omega_p} \approx \frac{\theta_s^2}{\theta_p^2} \approx \left(\frac{s_d}{s_2}\right)^2. \qquad (11.113)$$

Thus the total detected scatter flux and the integral SPR are both reduced as s_2 is increased. However, there is little benefit in making s_2 very much

larger than s_1; as soon as s_1 is negligible, $s_2 \approx s_d$ and the detector subtends approximately the same solid angle from the x-ray source as from the scattering element. Further increases in s_2 leave the SPR unchanged.

Of course, as discussed in Section 4.3.3, other considerations enter into the choice of s_1 and s_2 as well. If s_2/s_1 is increased, the focal spot of the x-ray tube must be smaller to maintain the same spatial resolution, but the resolution of the detector need not be as good [see (4.58) and (4.59)].

The third way to control scatter, the use of a grid, is illustrated in Fig. 11.7. In its simplest form, the grid is a series of parallel slats made of tungsten or other high-atomic-number material, and perhaps spaced apart with fiber-board or some other material with low-x-ray absorption. For an x-ray source a long distance away from the detector, the incident beam is essentially collimated. If $w \gg t$, very few of the unscattered photons strike the slats, and the primary image is largely unaffected by the grid. The only degradation of the primary image is a set of very fine lines, the shadows of the slats. This problem can be eliminated by making the grid frequency $1/w$ very large or by moving the grid uniformly parallel to the detector during exposure.

Scattered radiation, on the other hand, is no longer collimated, and most of it is blocked by the grid.

The calculation of the acceptance angle of the grid for scattered radiation is analogous to calculation of the geometric efficiency of a parallel-hole collimator for nuclear medicine. We showed in Section 4.5.4 that this efficiency is almost independent of the distance of the source from the face
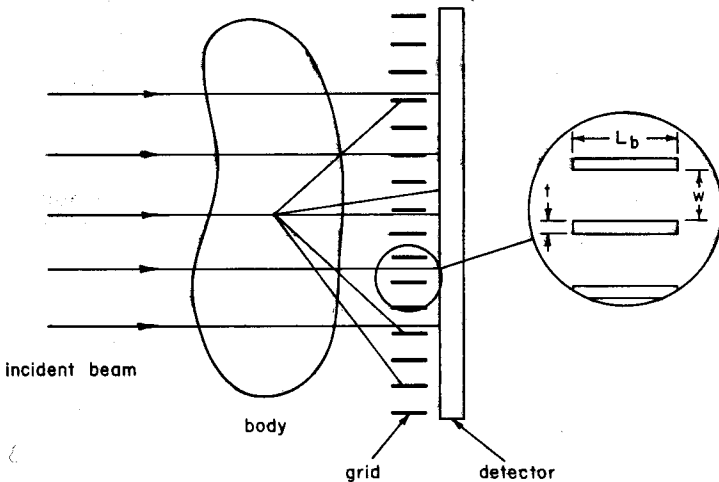

Fig. 11.7   A scatter-rejecting grid suitable for collimated radiation.

of the collimator. As the source moves away, the efficiency of each bore decreases but the number of bores that can accept radiation increases in a compensating manner [see (4.167)]. The same arguments apply to the grid, so we may as well calculate its acceptance solid angle by assuming the scatter source is in direct contact with the grid. Considering an isotropic distribution of scattered flux for simplicity, we find

$$\Omega_s = \int_0^\pi d\phi \int_{\pi/2 + W/2L_b}^{\pi/2 - W/2L_b} \sin\theta \, d\theta = \frac{\pi w}{L_b}. \tag{11.114}$$

If the slat thickness t is not negligible, this equation should also be multiplied by a packing fraction $w/(w + t)$. The quantity L_b/w is called the *grid ratio* (GR). Typical values of GR are 8 to 12.

Since a large detector in close proximity to a source subtends 2π steradians, we see that*

$$\frac{\text{SPR}_{\text{grid}}}{\text{SPR}_{\text{no grid}}} = \frac{\pi w/L_b}{2\pi} = \frac{1}{2\text{GR}}. \tag{11.115}$$

If the reduction factor of (11.115) is inadequate, two crossed grids can be used. This combination is equivalent to a two-dimensional collimator, for which $\Omega_s = w^2/L_b^2$, giving

$$\frac{\text{SPR}_{\text{grid}}}{\text{SPR}_{\text{no grid}}} = \frac{w^2/L_b^2}{2\pi} = \frac{1}{2\pi(\text{GR})^2} \tag{11.116}$$

The only reason not to make GR very large is the practical difficulty of making sure that the bores are properly aimed at the primary x-ray source. With a large GR, a slight tilt would greatly reduce the primary transmittance. A similar practical problem arises when the x-ray source is not a long distance from the grid. In that case it is common to use a *focused grid* as shown in Fig. 11.8.

Closely related to the grid is the scanning slit assembly shown in Fig. 11.9. The fore slit serves to define a narrow fan of x rays, while the aft slit rejects most of the scattered radiation. The two slits move at different velocities in such a way that they remain in line with the source. The time-averaged exposure on the detector is largely free of scatter.

The only drawback to this scheme is the relatively long time required to make a full exposure. Barnes and Brezovich (1979) have developed the method further by using several slits in each mask, creating what they call

---

* In practice, this equation somewhat overstates the reduction factor. Because of the forward peak in the scattering cross section and the finite size of the detector, the reduction will be less than 2GR. Furthermore, (11.115) applies only to the integral SPR; the grid is somewhat less effective, depending on the beam area, in reducing the local scatter-to-primary ratio.
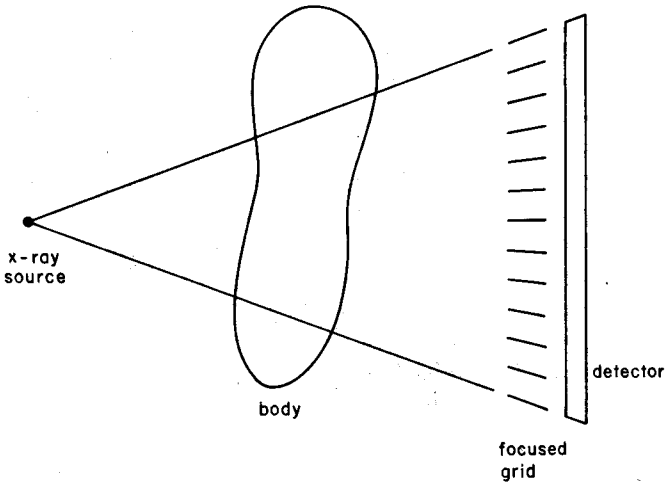
Fig. 11.8   Focused grid for scatter rejection when the x-ray source is at a finite distance from the detector.
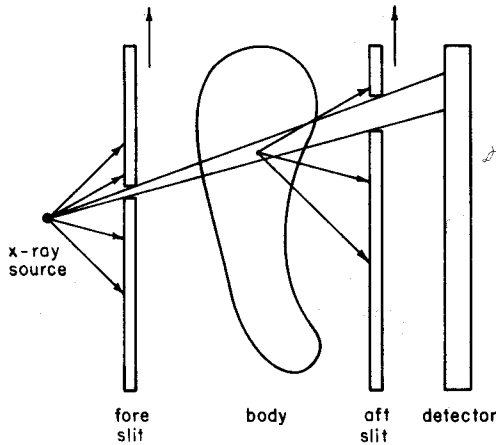

Fig. 11.9   Scanning slit assembly for scatter rejection.

a scanning multiple-slit assembly, or SMSA, and thereby reducing the exposure time. Some of their results are tabulated in Table 11.2.

Except for the scanning motion, the geometry of Fig. 11.9 is very similar to that of a fan-beam CT machine, which should also be largely immune to scatter. The old pencil-beam first-generation CT scanners, in fact, represent very nearly the best possible radiographic geometry for scatter rejection since the detector subtends such a small solid angle. But even with a fan beam, most of the scatter is out of the plane of the fan and hence misses

<div align="center">

TABLE 11.2[a]

Scatter-to-Primary Ratios for Various Scatter-Reduction
Techniques and X-Ray Tube Voltages[b]

</div>

Scatter-reduction technique	X-ray tube voltage			
	60 kVP	80 kVP	100 kVP	120 kVP
None	5.5	6.6	7.2	7.1
8:1 grid	0.72	1.0	1.2	1.4
12:1 grid	0.48	0.62	0.76	0.87
SMSA	0.16	0.20	0.22	0.22

[a] Taken from Barnes and Brezovich (1979).
[b] Using an 18-cm thick, 30 × 30 cm Lucite phantom.

the detector array. A collimator in front of the detectors improves matters further by eliminating certain multiply scattered photons.

The final method of scatter control in transmission radiography is optimization of the x-ray spectrum. High-energy photons interact with soft tissue predominantly by Compton scattering. Furthermore the differential scattering cross section is forward peaked (i.e., in the direction of the detector), so it might be expected that scattering problems would be particularly bad at high energies. However, higher energy photons have smaller total interaction cross sections and hence suffer fewer interactions in the body for a given number of transmitted photons. This effect reduces the scattered flux but also reduces the contrast in the primary image. Low-energy photons give a high-contrast primary image but are strongly absorbed in the body. The primary absorption process is photoelectric at very low energies ($\leqslant 40$ keV). Scattered radiation could therefore be greatly diminished just by keeping the photon energy below about 40 keV, but this would not be acceptable in terms of patient dose for radiographs of thick body parts.

The choice of an optimum photon energy or spectrum is thus a complicated trade-off involving noise, dose, detector characteristics, scatter, image contrast, and the specific diagnostic information needed. More discussion of the problem is given by Motz and Danos (1978) and Muntz (1979).

11.4.2 Emission Imaging

The geometrical remedies for scatter in transmission imaging—airgaps, grids, scanning slits, etc.—are not applicable in emission imaging. The fundamental difference is that we know the location of the primary source

in transmission imaging, but not in emission imaging. Photons coming from a particular volume element in the body in a nuclear image could equally well be photons originating from radioactive nuclei in that element or scattered photons from distant sources. There is no way to geometrically discriminate against scatter without the risk of also blocking desired primary photons.

On the other hand, nuclear imaging systems can use the powerful tool of energy discrimination. This method usually cannot be applied in transmission imaging because: (1) the photon arrival rate is much too high to allow processing individual photons; (2) the energy loss on each scattering event is very small at the low energies used in diagnostic radiology; (3) x-ray tubes emit a broad spectrum of energies, so it is impossible to reliably distinguish primary and scattered photons on the basis of their energy.

None of these difficulties applies in nuclear medicine. The isotopes used often emit most of their gamma rays with a single well-defined energy, and there is an appreciable energy loss on scatter. For example, the average loss for a 150-keV gamma ray is 27 keV, leaving the scattered photon an energy of 123 keV. There is no difficulty in discriminating between 123 and 150 keV with any well-designed scintillation detector, and semiconductor detectors can discriminate even much smaller differences. Furthermore the count rate in most nuclear medicine procedures is less than 10^5 counts/sec, allowing ample time for the electronics to process individual photons and accept or reject them on the basis of energy.

We may estimate the effect of energy discrimination on the integral SPR by using the single-scatter model. If the initial gamma-ray energy is $\mathscr{E}_0$ and the energy discriminator is set to reject photons below $\mathscr{E}_0 - \Delta\mathscr{E}$, then there is some maximum scattering angle $\theta_m(\Delta\mathscr{E})$ that could have occurred for any accepted photon. From (C.15)

$$\frac{1}{\mathscr{E}_0 - \Delta\mathscr{E}} - \frac{1}{\mathscr{E}_0} = \frac{1}{m_0 c^2}\{1 - \cos[\theta_m(\Delta\mathscr{E})]\}, \qquad (11.117)$$

or, if $\Delta\mathscr{E}/\mathscr{E}_0$ is small,

$$\frac{\Delta\mathscr{E}}{\mathscr{E}_0^2} \approx \frac{1}{m_0 c^2}\{1 - \cos[\theta_m(\Delta\mathscr{E})]\}. \qquad (11.118)$$

Since the primary photons are emitted isotropically, the distribution of once-scattered photons (in a thick scattering medium) is also isotropic even though the differential scattering cross section $d\sigma^C/d\Omega$ depends on scattering angle. Some small fraction of the scattered photons, determined by the geometry of the imaging system, are detected. This fraction is independent of the scattering angle θ and is the same as for unscattered photons. In other
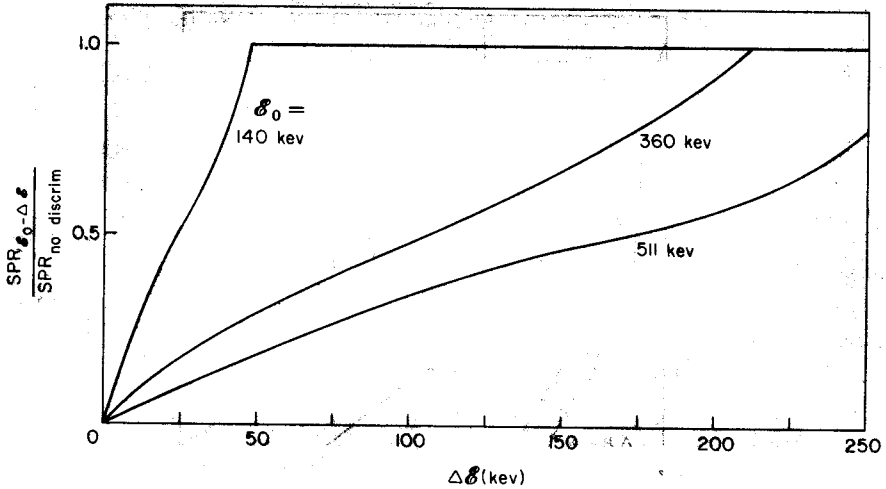
Fig. 11.10 Effect of energy discrimination on scatter-to-primary ratio in the single-scatter approximation [see (11.119)].

words, photons that have been scattered through, say, 30° are just as likely to be collected as unscattered photons since their initial directions were isotropically random. Therefore, the SPR with the energy threshold set at $\mathscr{E}_0 - \Delta\mathscr{E}$ is related to the SPR without energy discrimination by

$$\frac{\text{SPR}_{\mathscr{E}_0 - \Delta\mathscr{E}}}{\text{SPR}_{\text{no discrim}}} = \frac{2\pi \int_0^{\theta_m(\Delta\mathscr{E})} (d\sigma^C/d\Omega) \sin\theta \, d\theta}{2\pi \int_0^\pi (d\sigma^C/d\Omega) \sin\theta \, d\theta}. \tag{11.119}$$

If we use the low-energy limit (11.1) for $d\sigma^C/d\Omega$, this ratio of SPRs becomes

$$\frac{\text{SPR}_{\mathscr{E}_0 - \Delta\mathscr{E}}}{\text{SPR}_{\text{no discrim}}} = \tfrac{1}{2} - \tfrac{3}{8}\cos[\theta_m(\Delta\mathscr{E})] - \tfrac{1}{8}\cos^3[\theta_m(\Delta\mathscr{E})]. \tag{11.120}$$

More generally, (11.119) can be evaluated from the data given in Fig. C.7 and C.12. The ratio $\text{SPR}_{\mathscr{E}_0 - \Delta\mathscr{E}}/\text{SPR}_{\text{no discrim}}$ is plotted in Fig. 11.10 for several values of $\mathscr{E}_0$.

Many experimental studies of the effect of energy discrimination on imaging performance have been performed. A typical example is shown in Fig. 11.11. The general effect of better energy discrimination is to reduce the wings on the PSF and to restore the MTF at intermediate spatial frequencies. For this reason, there is considerable interest in building a nuclear camera based on semiconductor detectors, such as germanium, which have good energy resolution.
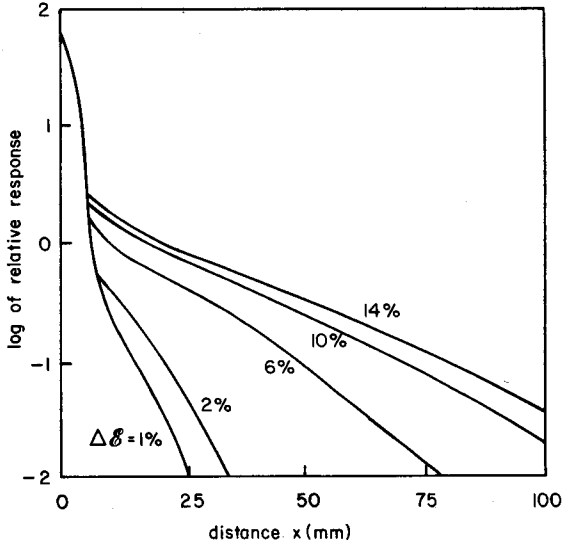
Fig. 11.11   Line spread function for a 140-keV source in a scattering medium for a detector with 3-mm spatial resolution and different degrees of energy discrimination. (Courtesy of J. W. Steidley.)

11.5   USES OF SCATTERED RADIATION

To this point we have regarded scattered radiation as something to be eliminated, but it is also possible to make good use of it. One way, called Compton radiography (Lale, 1959; Clark and van Dyk, 1969), is illustrated in Fig. 11.12. A ring source of ^{99m}Tc is used to irradiate a thin slice of the brain with 140-keV gamma rays. Except for multiple-scatter events, only 90° scattered rays can pass through the collimator. The energy window of the Anger camera is set at 109 keV, which is the energy of the gamma rays after 90° scattering.

Compton radiography provides a map of the Compton scattering cross-section, which is proportional to electron density, in the irradiated plane. This is basically the same information as in a CT scan at high energy, but Compton radiography may permit reduced patient dose. [See, however, the very pessimistic appraisal by Battista and Bronskill (1981).]

A variation on this theme, suggested by Leunbach (1977), is shown in Fig. 11.13. Here the incident radiation is collimated to a thin pencil beam which is viewed by two collimated detectors. For one position of the source and detectors, the system measures the electron density at the intersection
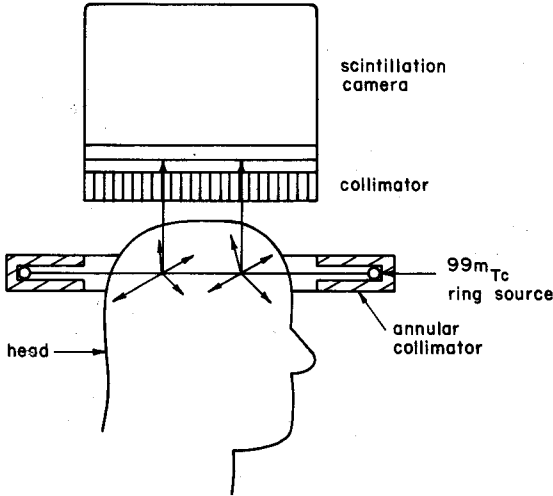
Fig. 11.12   Geometry for Compton radiography with a ring source.
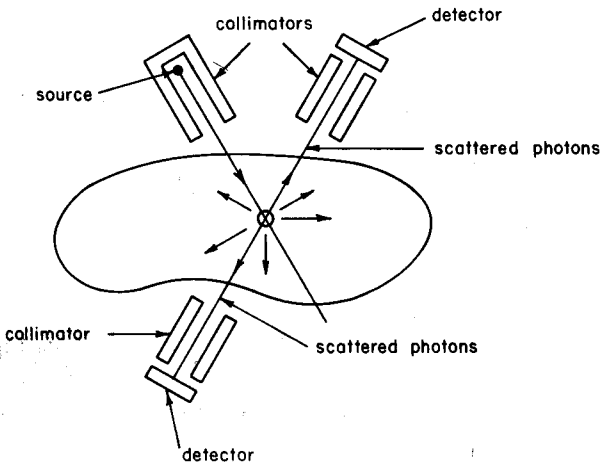

Fig. 11.13   Compton radiography system proposed by Leunbach (1977).

region defined by the incident beam and the field of view of the detectors. By scanning the whole source-detector assembly, a 2D or 3D image can be built up. This instrument can image any organ of the body in any section. A density discrimination of 1% is claimed.

It is also possible to form an image using fluorescent x rays rather than Compton scattered gamma rays (Hoffer *et al.*, 1969). In the system shown
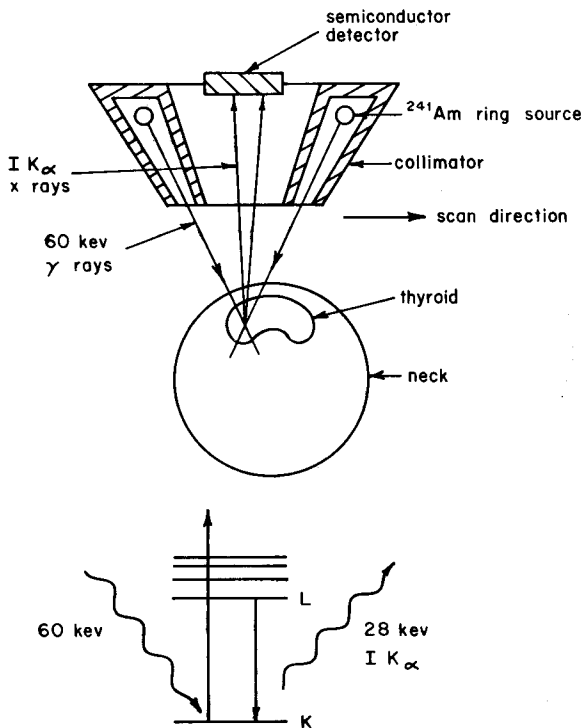
Fig. 11.14 Top: Basic geometry for fluorescent imaging of the thyroid. Bottom: Energy-level diagram. The 60 keV ^{241}Am gamma ray photoelectrically ionizes the K shell of an iodine atom, and the ensuing $L \rightarrow K$ transition produces a 28-keV iodine K x ray.

in Fig. 11.14, an intense ^{241}Am source generates 60-keV gamma rays that are collimated to a point in the thyroid gland. The natural iodine in the thyroid photoelectrically absorbs the 60-keV photons, creating vacancies in the K shell that are quickly filled with the emission of characteristic iodine K_α radiation at 28 keV. These fluorescent x rays are detected by a semiconductor detector. An image is built up by scanning the source-detector assembly.

This system provides unique information—the distribution of natural, stable iodine in the thyroid gland. It is thus complementary to nuclear medicine techniques using radioactive isotopes of iodine that measure the differential uptake of iodine by the thyroid.

In principle, fluorescent imaging could also be used for other high-atomic-number elements, but no other is present in the body in sufficient concentration. It is also possible to use stable isotopes as tracers in the same way as radioactive isotopes are used in nuclear medicine.